Modeling Biopotential Signals and Current Densities of Multiple Breast Cancerous Cells

Ahmed M. Hassan*, *Student Member, IEEE*, and Magda El-Shenawee, *Senior Member, IEEE*

***Abstract*—This study presents a model to simulate the electrophysiological activities of multiple Michigan Cancer Foundation-7 (MCF-7) cells, the most studied breast cancer cell line. The intercellular spacing of MCF-7 cells is estimated using the effective diffusion coefficient. Nonuniform finite-difference discretization is implemented to accommodate for the contrast in size between the intercellular spacing and the cell dimension. The model computes the amplitude and the spatiotemporal patterns of biopotentials and electric current densities at different cell division stages. The results show that the biopotentials increase proportionally to the number of cells, especially when all cells are in the hyperpolarization stage. Also, the results show significant electric current density in the intercellular gap between the cells.**

***Index Terms*—Bioelectric phenomena, biological cells, biophysics, cancer, Michigan Cancer Foundation-7 (MCF-7) cells.**

I. Introduction

In a comprehensive study, Berg *et al.* evaluated the performance of most of the current breast cancer diagnostic techniques such as mammography, clinical examination, ultrasound, and magnetic resonance imaging (MRI) [1]. The techniques were tested individually and in combinations. The study concluded that the highest sensitivity (99%) was achieved by combining diagnosis from mammography, clinical examination, and MRI at the expense of lower specificity (7%). The overall accuracy of combining mammography, clinical examination, and MRI was not higher than the use of mammography alone (only $\sim$70% in both cases) [1]. This study has motivated the current research to investigate the biophysics involved in cancerous Michigan Cancer Foundation-7 (MCF-7) cells that could lead in the future to an improved breast cancer detection modality.

In the late 1990s, the biopotential detection of breast cancer received large interest as a safe and harmless detection technique with a potential of differentiating between malignant and benign tumors [2], [3]. In a wide-scale study, involving 661 patients, the biopotential technique achieved a sensitivity of 90% for women with palpable lesions [2]. The main distinction of the biopotential detection of breast cancer lies on its association with electric signals generated by the tumor itself. Currently, there is a trend in the literature to advance biopotential detection of breast cancer [4]–[6].

Several articles were recently published to demonstrate the importance of bioelectromagnetic signals in the proliferations and regeneration of normal and cancerous cells [7]–[9]. This field has experienced resurgence in interest in order to explore novel techniques to control growth [7]–[9]. This rising interest has been fueled by the development of new experimental techniques to record and image the bioelectric signals generated by growing cells.

This study is an effort to augment these new experimental tools with a novel model that will help understand the mechanism by which breast cancerous cells generate electric signals as they grow. The current approach is analogous to other related research areas, such as gap junctional communication, where mathematical modeling of experimental data was reported for the quantitative analysis of the generated signals [9].

The objective of this study is to understand cancer electrophysiological phenomenon and, later on, propose an advanced biopotential technique for the early detection of breast cancer. For example, the model will provide better electrophysiological spatiotemporal patterns that could be used to improve positioning of the biopotential sensors on the breast [2].

The electrophysiological activities of a single MCF-7 cell were modeled in [10]. The model in [10] incorporated the membrane potential hyperpolarization of an MCF-7 cell during the Gap 1 (G1)/Synthesis (S) transition earlier reported in [11]. The membrane potential is the difference in the potential between the intracellular and extracellular media and is typically negative. The hyperpolarization is the phase when the membrane potential becomes more negative and the extracellular media becomes more positive [10]. The hyperpolarization was attributed to an increase in the permeability of the cell membrane to the positive potassium ions during this transition [12]. In addition, this transition is usually accompanied by an increase in the active intake of potassium ions as reported in other cancerous cells [13], [14].

However, in order to fully understand and analyze the electric signals recorded from breast cancer tumors, the model presented in [10] is extended in the current study to consider multiple cells. A better understanding of the signals' temporal and spatial patterns could be achieved by incorporating different distributions of the cancerous cells acting at different cell division stages, e.g., one cell is depolarization, another cell is hyperpolarizing, etc. The experimental study in [11]–[14] reported that cells at different stages exhibit different electric properties.

Manuscript received December 24, 2009; revised March 27, 2010 and April 20, 2010; accepted April 26, 2010. Date of publication May 10, 2010; date of current version August 18, 2010. This work was supported by the Doctoral Academy Fellowship at the University of Arkansas. *Asterisk indicates corresponding author.*

*A. M. Hassan is with the Department of Electrical Engineering, University of Arkansas, Fayetteville, AR 72701 USA (e-mail: amhassan@uark.edu).

M. El-Shenawee is with the Department of Electrical Engineering, University of Arkansas, Fayetteville, AR 72701 USA (e-mail: magda@uark.edu).

Color versions of one or more of the figures in this paper are available online at http://ieeexplore.ieee.org.

Digital Object Identifier 10.1109/TBME.2010.2049575

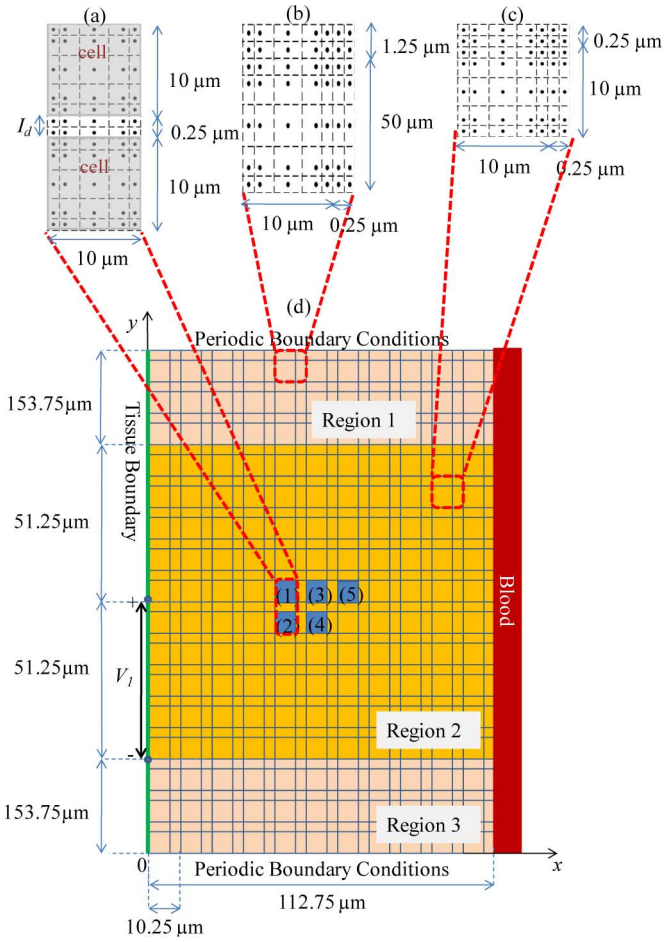

Fig. 1. (a) Two cells with the intercellular spacing. (b) Discretization in Regions 1 and 3. (c) Discretization in region 2. (d) Computational domain with five MCF-7 cells.

Section II describes the formulations and the nonuniform discretization scheme. Section III shows the numerical results, whereas Section IV outlines the conclusions.

II. Formulations

A uniform discretization of the domain in Fig. 1 would require 1600 pixels to model each cell leading to a drastic increase in the computational time. Therefore, a nonuniform discretization scheme is implemented, where only 25 pixels are used to model each cell and only ten pixels are used to model each intercellular spacing [see Fig. 1(a)]. The dots represent the pixels at which the ion concentrations and the biopotentials are calculated and the lines represent the boundaries of each pixel, where the electric current densities are calculated.

Considering multiple cells requires addressing the intercellular communication via gap junctions composed of proteins (connexins) [15]. It is well known that in primary tumors, there is a loss of gap junction intercellular between cells [15]–[17]. As a result, no electric coupling is assumed between the cancerous cells in this study.

The intercellular spacing is a key factor in the multiple cells model with estimated size of 0.25 μm (see Appendix A). The idea is based on modeling the MCF-7 tissue as a porous media with the cells acting as impermeable boundaries to glucose molecules and the intercellular spacing acting as the permeable medium.

Cell dynamics create nonhomogeneous ion concentrations that lead to diffusion-drift forces described by the Nernst–Plank, Poisson, and continuity equations [10]. The *implicit scheme* is used for the temporal discretization (t) of these equations to ensure stability [10], whereas the *nonuniform scheme* is implemented for the spatial discretization (x, y). Implicit discretization of the Poisson equation can be presented as shown in [10] as

$$\nabla^2 \phi^{t+1} = -\frac{F}{\varepsilon} \sum_m Z_m \left(C_m^t - \Delta t \nabla \vec{J}_m^{t,t+1} \right) \tag{1}$$

where ϕ represents the electrostatic potential (V), F represents the Faraday's constant (96485 C/mol), ε represents the permittivity of the plasma (80 ε_0 for water under quasi-static conditions), $\vec{J}_m$ represents the electric current density (moles/cm^2/s), C_m represents the concentration (moles/cm^3), and Z_m represents the signed charge for ion m.

Only four ions are considered due to their impact on the membrane potential reported in [10]; potassium C_{K^+}, sodium C_{Na^+}, chloride C_{Cl^-}, and negatively charged intracellular protein ions C_{A^-}. Since the proteins cannot penetrate the cell membrane, their concentration is assumed constant at 135 mM at all pixels inside the cell and zero concentration at all pixels outside the cell [10]. Both the intracellular and extracellular charged ions, C_{K^+}, C_{Na^+}, and C_{Cl^-}, are updated at each time step as described in [10]. Upon nonuniformly discretizing (1) in the x- and y-directions, as in [18], we obtain

$$\begin{aligned}\nabla^2 \phi^{t+1}(i,j) &= d^2\phi^{t+1}(i,j)/dx^2 + d^2\phi^{t+1}(i,j)/dy^2 \\ &= \frac{2}{h_{i,j}+h_{i,j+1}} \left(\begin{array}{l} \dfrac{\phi^{t+1}(i,j+1)}{h_{i,j+1}} + \dfrac{\phi^{t+1}(i,j-1)}{h_{i,j}} \\ -\phi^{t+1}(i,j)\dfrac{h_{i,j}+h_{i,j+1}}{h_{i,j}h_{i,j+1}} \end{array} \right) \\ &\quad + \frac{2}{g_{i,j}+g_{i+1,j}} \left(\begin{array}{l} \dfrac{\phi^{t+1}(i+1,j)}{g_{i+1,j}} + \dfrac{\phi^{t+1}(i-1,j)}{g_{i,j}} \\ -\phi^{t+1}(i,j)\dfrac{g_{i,j}+g_{i+1,j}}{g_{i,j}g_{i+1,j}} \end{array} \right)\end{aligned} \tag{2a}$$

$$\vec{\nabla} \vec{J}_m^{t,t+1} = \frac{J_{xm}(i,j+0.5) - J_{xm}(i,j-0.5)}{(h_{i,j}+h_{i,j+1})/2} + \frac{J_{ym}(i+0.5,j) - J_{ym}(i-0.5,j)}{(g_{i,j}+g_{i+1,j})/2} \tag{2b}$$

where

$$\begin{aligned}J_{xm}(i,j+0.5) = &\frac{-D_m(i,j+0.5)\left(C_m^t(i,j+1) - C_m^t(i,j)\right)}{h_{i,j+1}} \\ &- Z_m \mu_m (i,j+0.5) C_m^t(i,j+0.5) \\ &\times \frac{\phi^{t+1}(i,j+1) - \phi^{t+1}(i,j)}{h_{i,j+1}} + J_{a_{xm}}\end{aligned} \tag{2c}$$

where D_m represents the diffusion coefficient (cm^2/s) and μ_m represents the mobility ($\mathrm{cm}^2/\mathrm{V/s}$) of ion *m*, and

$$J_{xm}(i,j-0.5)=\frac{-D_m(i,j-0.5)\left(C_m^t(i,j)-C_m^t(i,j-1)\right)}{h_{i,j}} -Z_m\mu_m(i,j-0.5)\,C_m^t(i,j-0.5) \times\left(\phi^{t+1}(i,j)-\phi^{t+1}(i,j-1)\right)/h_{i,j}+J_{a_{xm}} \tag{2d}$$

in which, $h_{i,j+1}=x_{i,j+1}-x_{i,j}$, $h_{i,j}=x_{i,j}-x_{i,j-1}$, and $x_{i,j}, x_{i,j+1}$, and $x_{i,j-1}$ represent the *x*-coordinates of pixels (*i, j*), (*i, j*+1), and (*i, j*−1), respectively, and $g_{i+1,j}=y_{i+1,j}-y_{i,j}$, $g_{i,j}=y_{i,j}-y_{i-1,j}$, and $y_{i,j}, y_{i+1,j}$, and $y_{i-1,j}$ represent the *y*-coordinates of pixels (*i, j*), (*i*+1, *j*), and (*i*−1,*j*), respectively. Equations similar to (2c) and (2d) are obtained for J_{ym}.

The variable $J_{a_{xm}}$ in (2c) and (2d) represents the electric current density due to the active transport of ions by the sodium–potassium (Na^+–K^+) ATPase pump [10]. The active electric current densities are $J_{a_{x\mathrm{Na}^+}}$ for sodium and $J_{a_{x\mathrm{K}^+}}$ for potassium. The ratio between these current densities is 3:2, since the (Na^+–K^+) ATPase pump discharges three sodium ions for each two potassium ions it absorbs [10]. It is important to note that $J_{a_{xm}}$ is zero everywhere except at the cell boundaries. For example, if the top cell in Fig. 1(a) has its top-left pixel denoted as (*I*, *J*), $J_{a_{x\mathrm{Na}^+}}$ and $J_{a_{x\mathrm{K}^+}}$ are nonzero at the following boundaries; (*I*−0.5, *J*:*J*+4), (*I*+4.5,*J*:*J*+4), (*I*:*I*+4, *J*−0.5), and (*I*:*I*+4, *J*+4.5). The expressions for $J_{a_{x\mathrm{Na}^+}}$ and $J_{a_{x\mathrm{K}^+}}$ are given as shown in [10] as

$$J_{a_{x\mathrm{Na}^+}}=f_{\max}\left(\frac{C^t_{\mathrm{Na}^+_{-i}}}{C^t_{\mathrm{Na}^+_{-i}}+K_{\mathrm{Na}^+_{-i}}(1+C^t_{\mathrm{K}^+_{-i}}/K_{\mathrm{K}^+_{-i}})}\right)^3 \times\left(\frac{C^t_{\mathrm{K}^+_{-o}}}{(C^t_{\mathrm{K}^+_{-o}}+K_{\mathrm{K}^+_{-o}}(1+C^t_{\mathrm{Na}^+_{-o}}/K_{\mathrm{Na}^+_{-o}}))}\right)^2 \tag{3a}$$

and

$$J_{a_{x\mathrm{K}^+}}=-0.667J_{a_{x\mathrm{Na}^+}} \tag{3b}$$

where $f_{\max}$ is the maximum electric current density, $C^t_{\mathrm{Na}^+_{-i}}$ and $C^t_{\mathrm{K}^+_{-i}}$ refer to the intracellular sodium and potassium concentrations, respectively, and $C^t_{\mathrm{Na}^+_{-o}}$ and $C^t_{\mathrm{K}^+_{-o}}$ refer to the extracellular sodium and potassium concentrations, respectively. The $K_{\mathrm{Na}^+_{-i}}$, $K_{\mathrm{K}^+_{-i}}$, $K_{\mathrm{K}^+_{-o}}$, and $K_{\mathrm{Na}^+_{-o}}$ are defined as the *dissociation coefficients*, where their values are set to 0.2, 8.3, 0.1, and 18, respectively, as discussed in [10] and [19]. Expressions similar to (3) are used for $J_{a_{y\mathrm{Na}^+}}$ and $J_{a_{y\mathrm{K}^+}}$, respectively. By changing $f_{\max}$, the fluctuations in the ATPase pump activity are incorporated in the model. The fluctuations are the decrease in the ATPase pump activity at the beginning of the G1 phase and the increase in the ATPase pump activity at the G1/S transition as reported in [13] and [14].

During the cell division cycle, the membrane potential exhibits either depolarization (D), where the cell membrane becomes less negative, or hyperpolarization (H), where the cell membrane becomes more negative [10]. The depolarization of the membrane of the MCF-7 cell typically occurs at the beginning of the G1 stage of the cell division cycle, whereas the hyperpolarization of the cell membrane occurs at the G1/S transition of the cycle [11].

Both the depolarization (D) and the hyperpolarization (H) transitions are simulated using the computational domain shown in Fig. 1(d), which consists of four boundaries; the blood vessel on the right side of the domain, where the concentrations C_{K^+}, C_{Na^+}, and C_{Cl^-} are kept constant at 5, 155, and 160 mM, respectively, and the biopotentials are set to zero throughout the simulations [10]. The blood chloride concentration is set at 160 mM, which is higher than its typical value of ∼116 mM, to account for other negative ions. For example, in cancer patients, the blood concentration of sialic acid is ∼2.58 mM [20] and the concentration of lactic acids is ∼2.95 mM [21], which is much smaller than that of chloride ions. However, the concentration of sialic and lactic acids could be higher in the tissue in the vicinity of the tumor. Incorporating these ions in the model is feasible as a future research. The second boundary at $x=0$, where the zero flux boundary condition is imposed (i.e., $\partial\phi/\partial x=0$, $\partial C_m/\partial x=0$). The third and fourth boundaries at the top and bottom of the domain are assumed to have periodic boundary conditions [10].

Three main regions are marked in Fig. 1 as: region 1, region 2, and region 3. Regions 1 and 3 are inserted as padding to assure that the cancerous cells are adequately far from the periodic boundaries. This condition is essential in order to ensure that the periodic boundaries do not impact the electric signals. The second region is, where the MCF-7 cells are located and the biopotential difference V_1 between two points on the boundary $x=0$ is calculated. The discretization block 1 is used for regions 1 and 3 as shown in Fig. 1(b). The discretization block 2 is used for region 2 as shown in Fig. 1(c). The *y*-spacing in regions 1 and 3 is larger than the *y*-spacing in region 2 as shown in Fig. 1(b) and (c), which is found to be more efficient in extending the computational domain size without compromising the accuracy of the electrical signals or the required CPU time. Both regions 1 and 3 include 3×11 building blocks 1, while region 2 includes 10×11 building blocks 2 [see Fig. 1(d)].

Prior to simulating the depolarization (D) and the hyperpolarization (H) stages, an initial reference stage is created to simulate the cell state before division starts. The initial conditions of the reference stage are based on uniform distribution of potassium, sodium. and chloride ion concentrations as 5, 155, and 160 mM, respectively, similar to those used in the blood vessel pixels. In this stage, the biopotentials are initiated to zero at all pixels in the domain. The maximum electric current density, $f_{\max}$, is set equal to 0.5×10^{-9} $\mathrm{mM\cdot cm\cdot}s^{-1}$ in the reference stage. For the sodium, potassium, and chloride ions in (2), the diffusion $D_m\times 10^{-5}$ cm^2/s, and the mobility $\mu_m\times 10^{-4}\mathrm{cm}^2\cdot\mathrm{s}^{-1}\cdot\mathrm{V}^{-1}$ coefficients in plasma are given in Table I. The D_m and μ_m coefficients for plasma are set equal to those in water, since the plasma is mostly water [10]. Also, the diffusion $Db_m\times 10^{-11}$ cm^2/s and the mobility $\mu b_m\times 10^{-9}$ $\mathrm{cm}^2\cdot\mathrm{s}^{-1}\cdot\mathrm{V}^{-1}$ coefficients at the cells boundaries are given in Table I. The coefficients at the boundary and

TABLE I
DIFFUSION AND MOBILITY COEFFICIENTS USED IN THE INITIAL REFERENCE STAGE

D_{K^+}	D_{Na^+}	D_{Cl^-}	μ_{K^+}	μ_{Na^+}	μ_{Cl^-}
1.96	1.33	2.03	7.57	5.14	7.85
Db_{K^+}	Db_{Na^+}	Db_{Cl^-}	μb_{k^+}	μb_{Na^+}	μb_{Cl^-}
9.8	8.31	4.06	3.79	0.321	1.57

$f_{\max}$ are selected to satisfy the following two constraints: a realistic sodium ($\sim$12 mM) and potassium ($\sim$139 mM) ion concentration inside the cells [10] and a membrane potential of approximately ~ -45 mV typical of MCF-7 cells [11].

Once the cell reaches the steady state, the depolarization (D) and hyperpolarization (H) states are simulated by varying the parameters $f_{\max}$, Db_{K^+}, and μb_{K^+}. In the depolarization (D) state $f_{\max}$ is decreased to 25% of its initial value in the reference state, while Db_{K^+} and μb_{K^+} are decreased by a factor of 10. This causes the membrane potential to change to approximately ~ -15 mV at the end of the depolarization transition [10]. In addition, the intracellular potassium concentration decreases and the intracellular sodium concentration increases in the depolarization transition [10]. In the hyperpolarization (H) state $f_{\max}$, Db_{K^+}, and μb_{K^+} are increased back to their values in the reference state. The change in the maximum transport rate $f_{\max}$ is based on the neuroblastoma cells [13], [14], while the changes in Db_{K^+} and μb_{K^+} matches the measurements reported in [12].

III. NUMERICAL RESULTS

In all results, a cell size of 10 μm $\times$ 10 μm and an intercellular spacing of 0.25 μm are assumed. The results are obtained for the biopotential V_1 and the current densities $\vec{J}_m$ at the pixel boundaries (see Fig. 1).

A. The biopotential V_1

The potential difference between the point $x = 0$ μm, $y = 205$ μm and the point $x = 0$ μm, $y = 153.75$ μm is marked as V_1 in Fig. 1(d). In the clinical trials reported in [2] and [3], the potential difference is measured on patients using electrodes placed $\sim$2 cm apart versus 51.25 μm in the current study. This is not a limitation of the model, but a limitation of the available computational resources. Increasing the electrode separation will only affect the biopotentials magnitudes and not their patterns. Current investigation is focused on using the supercomputer platform to extend the computational domain to model the actual breast.

During the cell division stages, three electric transitions occur: 1) hyperpolarization (H); 2) depolarization (D); and 3) quiescence (Q). This will lead to 9 and 27 possible combinations of cell division stages when two and three MCF-7 cells are considered, respectively. When all cells are quiescent, no electric signals are generated. For clarity, only six combinations for two cells are shown in Fig. 2 and only seven combinations for three cells are shown in Fig. 3.

1) Two Cells (cell 1 and cell 2 in Fig. 1): In all results of Fig. 2, the V_1 of the single hyperpolarizing (H) cell 1 is used as a reference. Fig. 2(a) shows V_1 of two hyperpolarizing

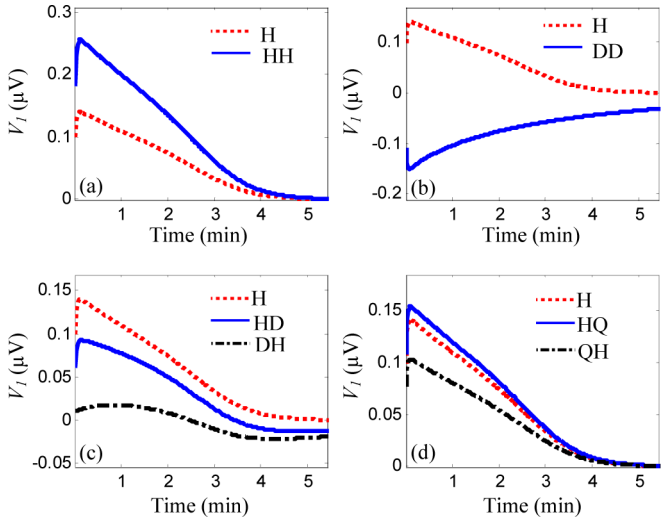

Fig. 2. V_1 versus time due to two cells for the (a) HH, (b) DD, (c) HD and DH, (d) HQ and QH, and (e) DQ and QD cases. Dotted line is for a single hyperpolarizing cell.

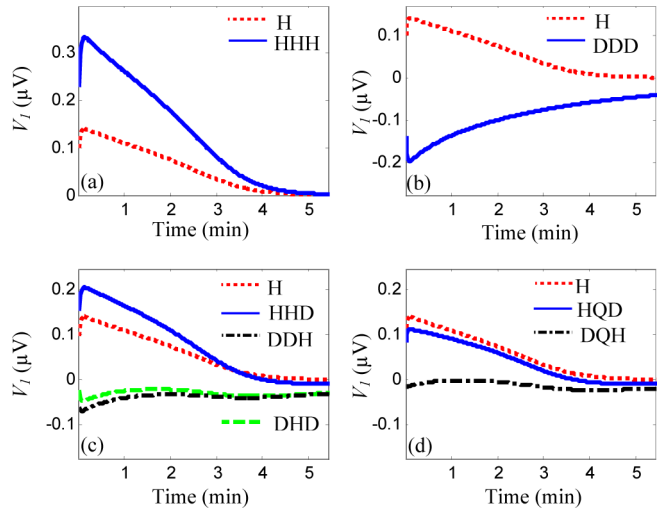

Fig. 3. V_1 versus time due to three cells for the (a) HHH, (b) DDD, (c) HHD, DHD, and DDH, (d) HQD and DQH, (e) HHQ and QQH, and (f) QQD and DDQ cases. Dotted line is for a single hyperpolarizing cell.

cells (HH) demonstrating a positive V_1 increasing to a peak of 0.255 μV versus 0.14 μV for the single cell. This indicates a ratio of 1.82. In both the 2 and 3 cells cases, the biopotential V_1 decays to zero as time progresses as the charge imbalance caused by either the H or the D or their combinations dissipates. However, if another transition follows, as one or more cells continue to divide, there will be another charge imbalance and the biopotential will be different for different transitions. Fig. 2(b) shows V_1 when the two cells are depolarizing (DD) demonstrating a negative V_1 compared to the single cell (H). Upon comparing Fig. 2(b) and Fig. 2(a), it can be seen that the magnitude of V_1 of the DD is smaller than that of the HH. A single depolarizing cell (not presented) generates a negative peak of -0.083 μV in V_1 versus a positive peak of 0.14 μV for a single hyperpolarizing cell. The reduction in V_1 for the depolarizing

cell could be attributed to the reduction in the coefficients Db_{K+} and μb_{K+} shown in Table I making the cell boundary less permeable to the intracellular potassium ions reducing their impact on the extracellular media. This differential permeability also explains the dominance of the hyperpolarization effect showing a positive voltage throughout the majority of the transition time in Fig. 2(c). In this case, cell 1 is hyperpolarizing and cell 2 is depolarizing (HD) or cell 1 could be depolarizing and cell 2 is hyperpolarizing (DH). Fig. 2(d) shows V_1 when cell 1 is hyperpolarizing and cell 2 is quiescent (HQ) that demonstrates an amplification of 9% compared with the reference (H). This could be due to the presence of a quiescent cell with semipermeable membrane acting as a boundary to the diffusing ions and restricting their motion to only one direction.

Upon comparing the HQ and QH shown in Fig. 2(d), it can be seen that switching the state of cell 1 and cell 2 affects the results depending on the proximity of the voltage recording points to these cells. It is important to mention that the notable difference could be due to the small scale used in this study.

2) Three Cells (cell 1, cell 2, and cell 3 in Fig. 1): All results of Fig. 3 show V_1 of the single hyperpolarizing (H) cell 1 as a reference. Fig. 3(a) shows V_1 when the three cells are hyperpolarizing (HHH) indicating a maximum ratio of 2.375. Fig. 3(b) shows negative V_1 when the three cells are depolarizing (DDD). Fig. 3(c) shows the results when cell 1 is hyperpolarizing, cell 2 is hyperpolarizing, and cell 3 is depolarizing (HHD); when cell 1 is depolarizing, cell 2 is hyperpolarizing, and cell 3 is depolarizing (DHD); and when cell 1 is depolarizing, cell 2 is depolarizing, and cell 3 is hyperpolarizing (DDH). The results show a larger V_1 in the HHD case compared with that of the DDH case, which generated the lowest V_1 among all cases, where there is a mixture of hyperpolarizing and depolarizing cells. Fig. 3(d) shows V_1 for the HQD and DQH in which cell 2 is quiescent. Due to space limit, the remainder of the 27 combinations is not shown.

Based on the nine combinations of the two cell divisions, the average of the peak of V_1, whether positive or negative, is 0.036 μV with $\pm 0.121 \mu$V standard deviation. While for the three cells and based on all 27 cell division combinations, the average of V_1 is 0.044 μV with ± 0.133 μV standard deviation. In calculating the average of V_1, equal probabilities for cell depolarization and hyperpolarization are assumed. However, in certain growth conditions the majority of cells might be in one division stage [22] leading to one transition being more probable than the other, which will be the focus of future investigation. The statistical results are shown in the whisker plot in Fig. 4(a) in which the circles indicate to the average values, while whiskers indicate to the minimum and maximum values. The results show that the average and the standard deviation of V_1 increase with increasing the number of cells. The observed increase is slight due to the small number of considered cells. Even though the increase in biopotential from two to three cells is relatively small, biopotentials do increase with the number of cells, or tumor size, as reported in [23]. The average of V_1 being positive is in agreement with the positive experimental measurements in [3] and [5]. However, other experimental studies reported that V_1 has negative values for other cancer cell lines [23].

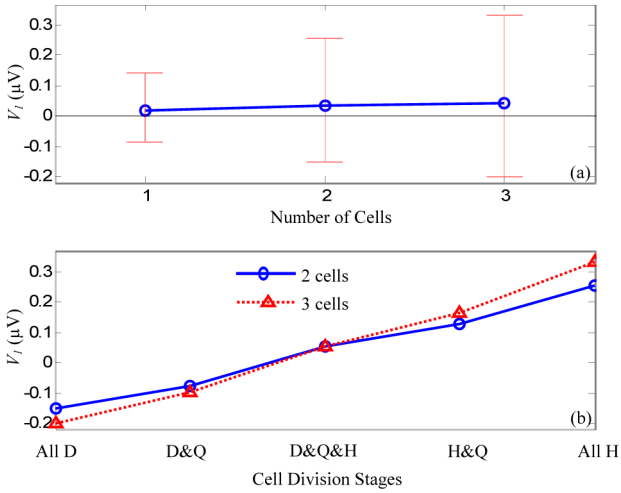

Fig. 4. (a) Whisker plot of V_1. The circles indicate to the average of all cell division combinations, while the error lines indicate to the maximum and minimum of V_1. (b) Average V_1 versus different cell division stages.

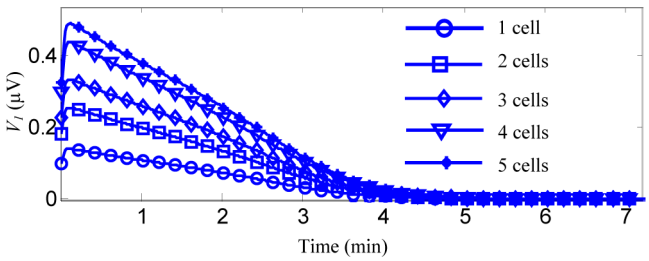

Fig. 5. V_1 versus time for all hyperpolarizing cells.

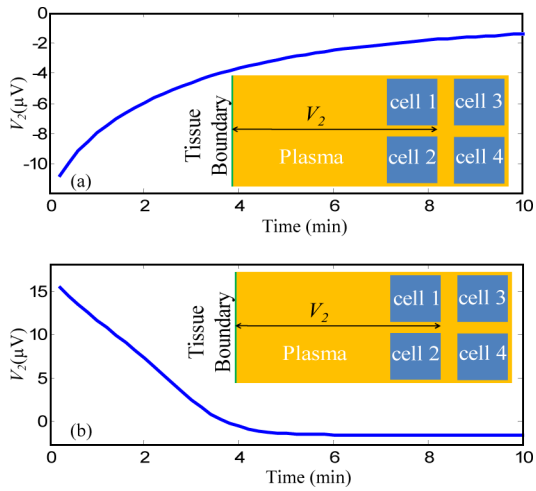

Fig. 6. Biopotential V_2 for (a) four depolarizing cells (DDDD) and (b) four hyperpolarizing cells (HHHH).

On the other hand, Fig. 4(b) shows V_1 versus the combination of cell division stages for two cells (circles) and three cells (triangles). For the two cell case, the average V_1 is calculated based on the x-axis label; "D&Q" means that the average is calculated based on the DQ and QD combinations, "D&Q&H" means the HD, DH, combinations, and "H&Q" means HQ and QH combinations. For the three cell case, the label "D&Q"

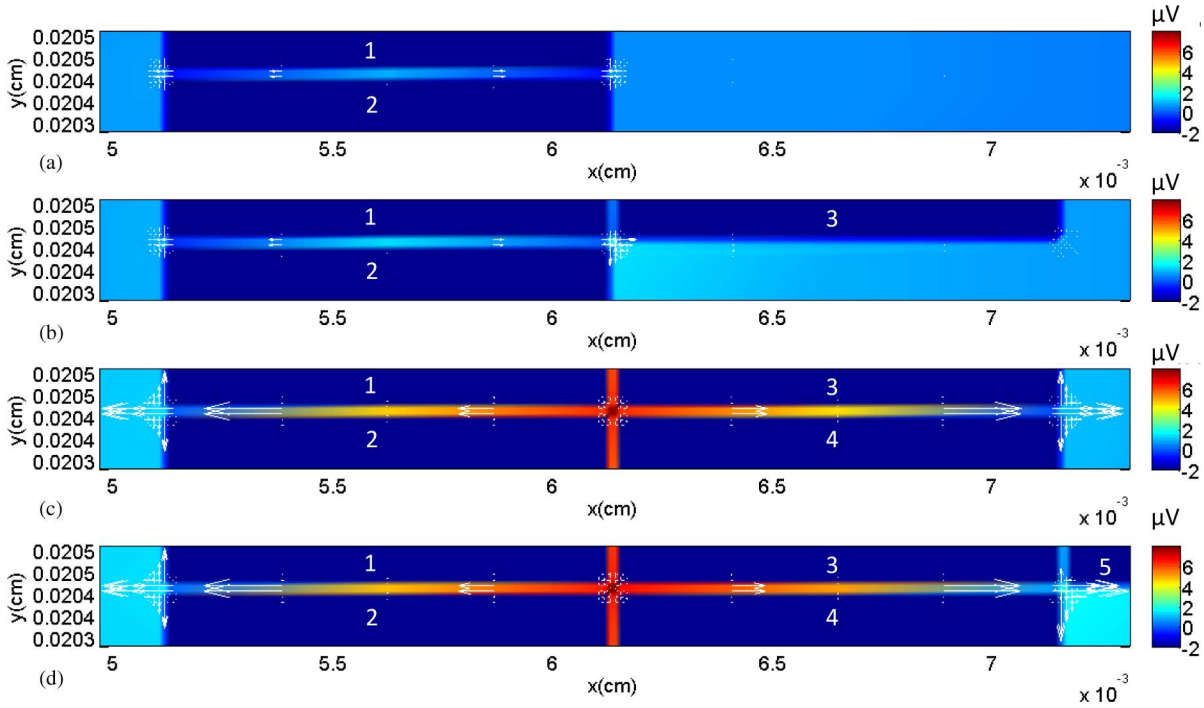

Fig. 7. Spatial distribution of biopotentials and electric current densities for (a) 2, (b) 3, (c) 4, and (d) 5 cells.

means the QQD, QDQ, DQQ, QDD, DQD, DDQ combinations, "D&Q&H" means the HHD, HDH, HDD, DHH, DHD, DDH, HQD, HDQ, QHD, QDH, DHQ, DQH combinations, and "H&Q" means the HHQ, HQH, QHH, HQQ, QHQ, and QQH combinations.

The aforementioned preliminary results suggest that the accuracy of using biopotential detection of breast cancer can be improved upon repeating the voltage recordings several times such that if in one recording the majority of the cells were depolarizing, it is likely that in the other recordings, the majority of the cell will flip to hyperpolarization, producing a larger positive signal.

3) Four and Five Cells [cell 1–cell 5 in Fig. 1(d)]: The number of combinations of cell division stages can be expressed as "3^n", where the 3 is due to the fact that three stages are considered (D, Q, and H) and n is the number of cells. Considering all combinations of cell division stages for four and five cells will lead to $3^4 = 81$ and $3^5 = 243$ cases, respectively. On the average, each simulation case requires $\sim$24 h on a 2.2-GHz processor with 8-GB of RAM leading to a prohibitive computational time. However, the results of the two and three cells indicate that the maximum biopotential is achieved when all cells are hyperpolarizing. Therefore, only the hyperpolarization case is considered for the four and five cells in Fig. 1(d). Fig. 5 shows a comparison of V_1 versus the time when all cells are hyperpolarizing. The results indicate that the behavior of V_1 is the same for all cells. The maximum V_1 is 0.140 μV, 0.2548 μV, 0.3318 μV, 0.4368 μV, and 0.4886 μV for one, two, three, four, and five cells, respectively.

Several studies in the literature involved the measurements of the biopotential difference between the inside and outside of the tumor [23]. Negative and positive biopotentials were recorded in different studies [23]. Therefore, the biopotential difference V_2 between a point near the center of the four cells and one point away from the tumor is plotted in Fig. 6. Fig. 6(a) shows V_2 when the four cells are depolarizing (DDDD) and Fig. 6(b) shows V_2 when the four cells are hyperpolarizing (HHHH). From Fig. 6(a), it can be seen that V_2 is negative and converges to a nonzero negative value. In Fig. 6(b), the biopotential V_2 starts as a positive value before converging to a negative value. From Fig. 6, it can be seen that the polarity of V_2 depends on the cell division stage.

B. Electric Current Density

The spatial distributions of the electric current densities and the biopotentials of the five hyperpolarizing cells are illustrated in Fig. 7(a)–(d) after 2.4 min from the start of the transition. A zero biopotential is assumed at the blood vessel to be the reference of the biopotentials in the surrounding plasma shown in Fig. 7(a)–(d). The color bar is only accurate in the extracellular media. The white arrows in the intercellular gap indicate to the overall electric current densities due to the potassium, sodium, and chloride ions, both active and passive. The currents everywhere else is insignificant. The lengths of these arrows correspond to the magnitude of the current density. All ions released in the intercellular spacing will accumulate because their movement is restricted to only the x-direction, since the cell membranes are acting as barriers. The results in Fig. 7(a) and (b) show that adding cell 3 does not significantly impact the biopotentials or the current densities in the intercellular gap between cell 1 and 2, but it impacts the biopotentials in its surrounding media. Cell 3 also creates a current density in the y-direction at the center of cell 1, cell 2, and cell 3. On the other

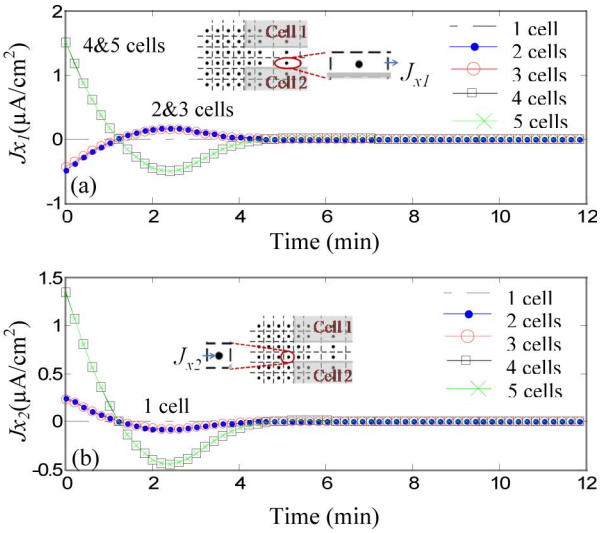

Fig. 8. x-component of the current density at (a) a pixel near the center of the intercellular gap (b) a pixel outside the intercellular spacing. All results are for the hyperpolarization transition.

hand, adding the fourth cell in Fig. 7(c) shows that the largest potential is observed at the center of the four cells. In addition, the current density in the intercellular spacing between cell 1 and cell 2 is magnified significantly in Fig. 7(c) compared with Fig. 7(a). The addition of the fifth cell in Fig. 7(d) increased the current density in the y-direction at the center of cell 3, cell 4, and cell 5 compared with Fig. 7(c) due to the intercellular spacing between cell 3 and cell 5.

The x-components of the current density are plotted versus the time at the two pixels identified in Fig. 8(a) and (b). The current density J_{x1} calculated at a pixel near the center of the intercellular spacing is shown in Fig. 8(a), while the current density J_{x2} calculated at a pixel near the boundary of the intercellular spacing is shown in Fig. 8(b). The current densities of a single cell are insignificant compared to those of multiple cells. Fig. 8(a) shows that the current at the center of the intercellular gap reverses its direction when four or five cells are added. This observation is due to the shift of the maximum potential from the center of the intercellular gap between cell 1 and cell 2 to the center of the four cells as shown in Fig. 7(c). Interestingly, when multiple cells are considered, the current densities increased by at least a factor of three, whereas the biopotentials increased by a factor of almost two.

IV. Conclusion

A novel electrophysiological model to compute the biopotentials and the electric current densities of multiple MCF-7 cells immersed in plasma was developed in this study. This model was used to simulate the membrane potential depolarization, which typically occurs at the beginning of the G1 stage, and the hyperpolarization, which typically occurs at the G1/S transitions [11], [13], [14]. The results were based on few cells to prove the concept that the overall extracellular biopotential is positive. This could be explained by the domination of the positive extracellular biopotentials during the hyperpolarization transition over the extracellular negative biopotentials during the depolarization transition. The average of the generated biopotentials showed an increasing trend as the number of cells increased. The results also show an increase in the electric current densities in the intercellular spacing. The observed amplification of the electric current densities in the intercellular spacing was larger than that of the extracellular biopotential.

Ongoing research aims to incorporate hundreds of MCF-7 cells using the supercomputer upon implementing the message passing interface parallelization technique. The proposed model will be extended to include other biological features such as the interactions with the extracellular matrix components as well as other tumor growth characteristics. The formation of multilayers can also be achieved by updating the model equations into three dimensions. This will cause the computational cost to increase significantly, but can be achieved upon using the peta-scale supercomputers.

Appendix A

The study in [24] reported an estimate of 1×10^{-7} for the effective diffusion coefficient (D_{eff}) of glucose in tissue composed of MCF-7 cells, which is a macroscopic property affected by the intercellular spacing. The intercellular spacing filled with plasma is mainly composed of water with glucose diffusion coefficient $D_0 = 6.7 \times 10^{-6}$ [25]. The relationship between D_{eff} and D_0 is given by $D_{\text{eff}} = D_0 \delta \varepsilon / \tau$ in [26], where δ, ε, and τ are the *constrictivity*, *porosity*, and *tortuosity* factors, respectively. The δ factor defines the reduction in D_{eff} when the size of the diffusing molecule is comparable to the size of the intercellular spacing. When the size of the diffusing molecule is much smaller than the intercellular spacing, δ can be assumed 1 [27]. The porosity ε is defined as the ratio between the area of the medium where the glucose molecules can diffuse (i.e., the intercellular spacing) and the area where the glucose molecules are impermeable (i.e., the MCF-7 cells) [26]. The tortuosity τ is the ratio between the actual length the glucose molecules travel with and without the presence of the MCF-7 cells [26]. An empirical formula was developed to calculate τ as a function of ε; $\tau = 1 - p \ln(\varepsilon)$, where the optimum p factor was found to equal 0.77 ± 0.03 [28]. Assuming that the size of the MCF-7 cell is 10 μm $\times$ 10 μm as done in [10], the unit cell in the porous MCF-7 tissue will have an average area of $(10\ \mu\text{m} + I_d)^2$. The porosity ε can be calculated as the ratio between the area of the intercellular fluid and the area of the unit cell expressed as $\varepsilon = \left((10\ \mu\text{m} + I_d)^2 - (10\,\mu\text{m})^2\right) / (10\ \mu\text{m} + I_d)^2$ from which the intercellular spacing I_d can be estimated to be $\sim$0.25 μm. Notice that this value of the intercellular spacing is significantly larger than the size of the glucose molecule (12.474 Å) presented in [29], which justifies setting δ to unity in this study.

References

[1] W. Berg, L. Gutierrez, M. NessAiver, W. Carter, M. Bhargavan, R. Lewis, and O. Ioffe, "Diagnostic accuracy of mammography, clinical examination, US, and MR imaging in preoperative assessment of breast cancer," *Radiology*, vol. 233, pp. 830–849, Dec. 2004.

[2] R. Cuzick, Holland, V. Barth, R. Davies, M. Faupel, I. Fentiman, H. Frischbier, J. LaMarque, M. Merson, V. Sacchini, D. Vanel, and U. Veronesi,

"Electropotential measurements as a new diagnostic modality for breast cancer," *Lancet*, vol. 352, pp. 359–363, 1998.
[3] M. Fukuda, K. Shimizu, N. Okamoto, T. Arimura, T. Ohta, S. Yamaguchi, and M. L. Faupel, "Prospective evaluation of skin surface electropotentials in Japanese patients with suspicious breast lesions," *Jpn. J. Cancer Res.*, vol. 87, no. 10, pp. 1092–1096, 1996.
[4] E. Ng, W. Ng, L. Sim, and U. R. Acharya, "Numerical modelling of biopotential field for detection of breast tumour source," *Comput. Biol. Med.*, vol. 37, no. 8, pp. 1121–1132, 2007.
[5] S. V. Sree, E. Ng, and U. R. Acharya, "Data mining approach to evaluating the use of skin surface electropotentials for breast cancer detection," *Technol. Cancer Res. Treat.*, vol. 9, no. 1, pp. 95–106, 2010.
[6] R. J. Davies. "Method and system for detecting electrophysiological changes in pre-cancerous and cancerous breast tissue and epithelium", U.S. Patent 7 630 759, Dec. 8, 2009.
[7] C. McCaig, A. Rajnicek, B. Song, and M. Zhao, "Controlling cell behavior electrically: Current views and future potential," *Physiol. Rev.*, vol. 85, pp. 943–978, 2005.
[8] S. Sundelacruz, M. Levin, and D. Kaplan, "Role of membrane potential in the regulation of cell proliferation and differentiation," *Stem Cell Rev.*, vol. 5, no. 3, pp. 231–246, 2009.
[9] A. Esser, K. Smith, J. Weaver, and M. Levin, "Mathematical model of morphogen electrophoresis through gap junctions," *Dev. Dyn.*, vol. 235, pp. 2144–2159, 2006.
[10] A. M. Hassan and M. El-Shenawee, "Diffusion-drift modeling of a growing breast cancerous cell," *IEEE Trans. Biomed. Eng.*, vol. 56, no. 10, pp. 2370–2379, Oct. 2009.
[11] J. Strobl, W. Wonderlin, and D. Flynn, "Mitogenic signal transduction in human breast cancer cells," *Gen. Pharmacol.*, vol. 26, no. 8, pp. 1643–1649, 1995.
[12] W. Wonderlin, K. Woodfork, and J. Strobl, "Changes in membrane potential during the progression of MCF-7 human mammary tumor cells through the cell cycle," *J. Cell. Phys.*, vol. 165, pp. 177–185, 1995.
[13] C. Mummery, J. Boonstra, L. Tertoolen, P. Van Der Saag, and S. De Laat, "Modulation of functional and optimal (Na+-K+)ATPase activity during the cell cycle of neuroblastoma cells," *J. Cell. Physiol.*, vol. 107, no. 1, pp. 1–9, 1981.
[14] J. Boonstra, C. Mummery, L. Tertoolen, P. Van Der Saag, and S. De Laat, "Cation transport and growth regulation in neuroblastoma cells. Modulations of K +transport and electrical membrane properties during the cell cycle," *J. Cell. Physiol.*, vol. 107, no. 1, pp. 75–83, 1981.
[15] E. McLachlan, Q. Shao, and D. Laird, "Connexins and gap junctions in mammary gland development and breast cancer progression," *J. Membr. Biol.*, vol. 218, pp. 107–121, 2007.
[16] N. Wei, M. Mi, and Y. Zhou, "Influences of lovastatin on membrane ion flow and intracellular signaling in breast cancer cells," *Cell. Mol. Biol. Lett.*, vol. 12, pp. 1–15, 2007.
[17] C. Sáez, L. Velásquez, M. Montoya, E. Eugenín, and M. Alvarez, "Increased gap junctional intercellular communication is directly related to the anti-tumor effect of all-trans-retinoic acid plus tamoxifen in a human mammary cancer cell line," *J. Cell. Biochem.*, vol. 89, pp. 450–461, 2003.
[18] P. Moin, *Fundamentals of Engineering Numerical Analysis*. Cambridge, MA: Cambridge Univ. Press, 2001.
[19] V. Lew and R. Bookchin, "Volume, pH, and ion-content regulation in human red cells: Analysis of transient behavior with an integrated model," *J. Membr. Biol.*, vol. 92, pp. 57–74, 1986.
[20] N. Stefenelli, H. Klotz, A. Engel, and P. Bauer, "Serum sialic acid in malignant tumors, bacterial infections, and chronic liver diseases," *J. Cancer Res. Clin. Oncol.*, vol. 109, pp. 55–59, 1985.
[21] T. Nishijima, M. Nishina, and K. Fujiwara, "Measurement of lactate levels in serum and bile using proton nuclear magnetic resonance in patients with hepatobiliary diseases: Its utility in detection of malignancies," *Jpn. J. Clin. Oncol.*, vol. 27, no. 1, pp. 13–17, 1997.
[22] R. Sutherland, R. Hall, and I. Taylor, "Cell Proliferation Kinetics of MCF-7 Human Mammary Carcinoma Cells in Culture and Effects of Tamoxifen on Exponentially Growing and Plateau-Phase Cells," *Cancer Res.*, vol. 43, pp. 3998–4006, Sep. 1983.
[23] D. Miklavčič, G. Sersa, S. Novakovic, and S. Rebersek, "Tumor bioelectric potential and its possible exploitation for tumor growth retardation," *J. Bioelectricity*, vol. 9, no. 2, pp. 133–149, 1990.
[24] H. Frieboes, M. Edgerton, J. Fruehauf, F. Rose, L. Worrall, R. Gatenby, M. Ferrari, and V. Cristini, "Prediction of drug response in breast cancer using integrative experimental/computational modeling," *Cancer Res.*, vol. 69, no. 10, pp. 4484–4492, 2009.
[25] D. Lide, *CRC Handbook of Chemistry and Physics*, 88th ed. Boca Raton, FL: CRC Press, Jun. 2005.
[26] C. Salmas and G. Androutsopoulos, "A novel pore structure tortuosity concept based on nitrogen sorption hysteresis data," *Ind. Eng. Chem. Res.*, vol. 40, pp. 721–730, 2001.
[27] P. Grathwohl, *Diffusion in Natural Porous Media: Contaminant Transport, Sorption/Desorption and Dissolution Kinetics*, 1st ed. New York: Springer-Verlag, 1998.
[28] M. Matyka, A. Khalili, and Z. Koza, "Tortuosity-porosity relation in porous media flow," *Phys. Rev. E*, vol. 78, pp. 026306-1–026306-8, 2008.
[29] R. Netrabukkana, K. Lourvanij, and G. Rorrer, "Diffusion of glucose and glucitol in microporous and mesoporous silicate/aluminosilicate catalysts," *Ind. Eng. Chem. Res.*, vol. 35, pp. 458–464, 1996.

Ahmed M. Hassan (S'07) received the B.Sc. degree (with highest honors) and the M.Sc. degree both in electronics and communications engineering from Cairo University, Cairo, Egypt, in 2004 and 2006, respectively. He is currently working towards the Ph.D. degree in the Electrical Engineering Department, University of Arkansas, Fayetteville in breast cancer modeling and bioelectromagnetics.

Mr. Hassan is the recipient of the Doctoral Academy Fellowship at the University of Arkansas.

Magda El-Shenawee (M'91–SM'02) received the Ph.D. degree in electrical engineering from the University of Nebraska-Lincoln, Lincoln, in 1991.

She was a Research Associate at the Center for Electro-Optics, University of Nebraska-Lincoln during 1992–1994, where she was involved in the research on the enhanced backscatter phenomenon from random rough ground surfaces. She was involved in research at the National Research Center, Cairo, Egypt, during 1994–1996, and at the University of Illinois, Urbana-Champaign, during 1997–1999. During 1999–2001, she was a Member of the Multidisciplinary University Research Initiative team, Northeastern University, Boston, MA, where she was involved in the research on the antipersonnel landmine detection . She joined the University of Arkansas, Fayetteville as an Assistant Professor in 2001, where she is currently a Professor of electrical engineering. Her research interests include computational electromagnetics, biomedical engineering application to breast cancer research using biopotentials, biomagnetics, biological tumor growth modeling, and microwave imaging algorithms of breast cancer.

Dr. El-Shenawee is a member of Eta Kappa Nu electrical engineering honor society.